DNS of laminar-turbulent transition in swept-wing boundary layers

By L. Duan†, M. Choudhari‡ AND F. Li‡

Direct numerical simulation (DNS) is performed to examine laminar to turbulent transition due to high-frequency secondary instability of stationary crossflow vortices in a subsonic swept-wing boundary layer for a realistic natural-laminar-flow airfoil configuration. The secondary instability is introduced via inflow forcing and the mode selected for forcing corresponds to the most amplified secondary instability mode that, in this case, derives a majority of its growth from energy production mechanisms associated with the wall-normal shear of the stationary basic state. An inlet boundary condition is carefully designed to allow for accurate injection of instability wave modes and minimize acoustic reflections at numerical boundaries. Nonlinear parabolized stability equation (PSE) predictions compare well with the DNS in terms of modal amplitudes and modal shape during the strongly nonlinear phase of the secondary instability mode. During the transition process, the skin friction coefficient rises rather rapidly and the wall-shear distribution shows a sawtooth pattern that is analogous to the previously documented surface flow visualizations of transition due to stationary crossflow instability. Fully turbulent features are observed in the downstream region of the flow.

1. Introduction

Skin-friction drag accounts for approximately one half of the total drag for business jets and long-haul transport aircraft (Washburn 2011). Transition delay via laminar flow technology is an important component of drag reduction technologies. Although system studies have shown that 9%−10% fuel savings can be achieved by delaying boundary-layer transition over major aerodynamic surfaces, the projected benefits can be significantly offset by uncertainties in transition prediction. In order to enable usable and robust designs for Natural Laminar Flow (NLF) and Hybrid Laminar Flow Control (HLFC), it is critical to link transition prediction to high-fidelity aircraft design tools (Washburn 2011). One important technical gap that prevents accurate transition prediction in swept-wing boundary layers is the transition due to crossflow instability. Due to multiple possible breakdown scenarios, crossflow transition cannot be accurately predicted by tools based on linear stability alone, and a hierarchical approach that accounts for receptivity and nonlinear phases of transition is needed (Choudhari *et al.* 2003).

The process of laminar breakdown during crossflow-dominated transition is often associated with high-frequency secondary instabilities of finite amplitude crossflow modes. Recent work (Malik *et al.* 1999; Li *et al.* 2011) has shown that transition predictions accounting for the amplification of secondary instabilities can lead to reduced uncertainty in transition prediction. However, multiple families of secondary instabilities are known to exist, and, therefore, the questions of which of those families may lead to transition in

† Department of Mechanical and Aerospace Engineering, Missouri University of Science and Technology
‡ NASA Langley Research Center

a given case and what are the associated breakdown mechanisms have not been answered as yet.

DNS is an important ingredient in the hierarchical prediction approach that can be used to study complete transition due to crossflow vortices in order to understand the breakdown mechanisms responsible for the onset of transition. DNS is crucial to guiding and validating the application of lower-fidelity tools in complex 3D flows and will eventually serve as a proxy to controlled experiments in a fully quantifiable disturbance environment. Earlier DNS of boundary layer flows concentrated either on the linear and early nonlinear regime of transition (Rist & Fasel 1995) or on the fully developed turbulent boundary layers (Moin & Kim 1982; Spalart 1988). More recent DNS studies simulated the entire transition regime to a fully turbulent boundary layer, including both bypass transition due to high-intensity free-stream turbulence (Wu & Moin 2009; Nagarajan *et al.* 2007; Ovchinnikov *et al.* 2008) and the transition processes associated with linear instabilities such as the oblique breakdown of first mode waves in a two-dimensional supersonic boundary layer (Jiang *et al.* 2006; Mayer *et al.* 2011) or the transition due to secondary instabilities of Tollmien-Schlichting waves in a low-speed flat plate boundary layer (Sayadi *et al.* 2013). In terms of crossflow-induced transition in a three-dimensional boundary layer, the present authors (Choudhari *et al.* 2013; Duan *et al.* 2013) performed preliminary DNS studies of laminar breakdown initiated by the secondary instability of stationary crossflow vortices in a swept-wing flow configuration that is relevant to subsonic transports. These simulations illustrated several important features of crossflow transition due to secondary instabilities: a long saturation zone before the onset of transition, a rapid rise in skin friction during the laminar breakdown, and a 'sawtooth'-patterned transition front that is similar to the surface visualizations in previous wind-tunnel experiments using naphthalene sublimation. However, due to the limited domain size in the streamwise direction, the generated turbulence was still nascent, indicating a persistent memory of the original crossflow vortex within the DNS domain.

The present work reports a refined DNS of laminar breakdown initiated by a single secondary instability mode associated with wall-normal shear of the stationary vortices for the same swept-wing flow configuration with a systematic assessment of the influence of boundary conditions. In addition, the DNS dataset is utilized to assess the validity of nonlinear PSE during the linear and nonlinear phases of secondary mode evolution and to shed light on whether a single secondary instability mode leads to a state we recognize as a fully turbulent boundary layer.

1.1. *Flow conditions and numerical methodology*

The work in this paper considers the boundary layer over a swept NLF wing that was designed by Texas A & M University (TAMU) (Belisle *et al.* 2010). The wing is designed to achieve natural laminar flow over both suction and pressure surfaces at the design angle-of-attack of 0 degrees, with target conditions of $\mathrm{M}_\infty = 0.75$ at an altitude of $H = 40$ kft, a chord Reynolds number, Re_{c_s}, between 15 and 20 million, and a leading-edge sweep angle, Λ, of 30°. The free flight conditions for the work described in this paper are summarized in Table 1. The current DNS studies the boundary layer over the suction surface of the TAMU airfoil at the off-design angle-of-attack of −1 degrees. The focus is on the boundary layer in the late-transitional and turbulent regions. Transition is triggered by the Y-Mode secondary instability of the stationary crossflow vortex, with a spanwise wave length of $\lambda_y = 8$ mm. Here, the letter notation for different classes of secondary instability modes follows the suggestion of Malik *et al.* (1999) with Y-mode

TABLE 1. Free flight conditions for the DNS.

M_∞	U_∞(m/s)	ρ_∞(kg/m^3)	T_∞(K)	c(m)	Re_{c_s}($\times 10^6$)
0.75	221.28	0.302	216.65	3.1676	17.2

denoting the high-frequency mode II induced by the local maximum of the wall-normal gradient. The details of the methodology employed for computing the mean boundary-layer flow over the suction surface of the airfoil, the linear and nonlinear development of the primary crossflow vortex, and the secondary instability predictions are summarized in Li *et al.* (2010).

The DNS employs a non-orthogonal vortex-aligned coordinate system (Figure 1) and solves the compressible Navier-Stokes equations in generalized curvilinear coordinates. The details of the non-orthogonal vortex-aligned coordinate system and numerical methods are summarized in Duan *et al.* (2013). The DNS simulates the physical boundary layer over the TAMU airfoil extending from $0.5 < x/c < 0.622$ in the streamwise direction, which covers the entire transition region starting from the nearly stationary flow upstream to a significantly long region of fully developed turbulent flow near the downstream end. At the inlet, a three-dimensional laminar profile corresponding to the finite-amplitude stationary crossflow vortex is specified as the basic state (Figure 2a), which is superimposed by the selected Y-mode secondary instability wave as an unsteady disturbance (Figure 2b). The amplitude of the Y-mode instability wave, measured by the maximum of the root-mean-square streamwise velocity fluctuation over the local cross-section, is 0.2885 m/s at the inlet ($x/c = 0.5$). Compared with the previous simulation (Duan *et al.* 2013) that ends at $x/c = 0.572$, the current simulation grid extends deeper into the turbulent region to ensure an adequate streamwise extent for computing turbulence statistics across the region of nascent and fully developed turbulence.

The boundary conditions of the DNS are specifically designed for injecting instability waves (with the exact modal shape) at the inlet and for minimizing acoustic reflections at numerical boundaries (Figure 3). The secondary instability wave is injected through a near-wall disturbance injection zone where the Dirichlet boundary condition applied. The height of the disturbance injection region is about twice that of the inlet boundary-layer thickness ($2\delta_i$), which accounts for less than 1% of the height of the inlet boundary. An inlet sponge zone (Bodony 2006) is added above the near-wall region for the rest of the inlet. A fringe zone (Breuer 2007) is added from $0.442 < x/c < 0.5$, where the basic state at the physical inlet ($x/c = 0.5$) is imposed to allow for sufficient streamwise development of the injected secondary instability wave. As a result, a relatively small amplitude of the input instability wave is required to achieve transition in the downstream. For the outflow and top boundaries, sponge zones similar to the inlet sponge are added from $0.622 < x/c < 0.646$ and $129 < z/\delta_i < 246$ to avoid reflections of disturbance. For all the sponges, the basic state (without the superposition of the secondary instability wave) is used as the sponge reference. The width of the sponges is comparable to or larger than the wavelength of the low-frequency outgoing acoustic waves, and the strength of the sponges is adjusted such that the amplitude of the outgoing acoustic waves decays over the entire sponge length. The effect of chosen boundary conditions in minimizing acoustic reflection as well as determining sponge parameters has been assessed systematically by numerical experiments (Section 1.2). On the wall, no-slip conditions are applied for the three velocity components and an isothermal condition is used for the temperature,

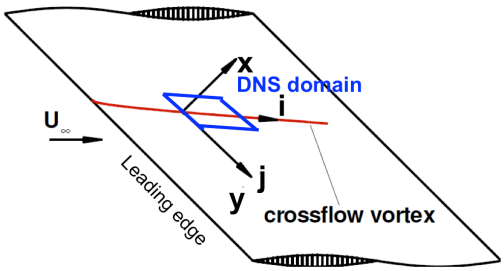

FIGURE 1. Sketch of vortex-aligned computational domain for the DNS simulation.

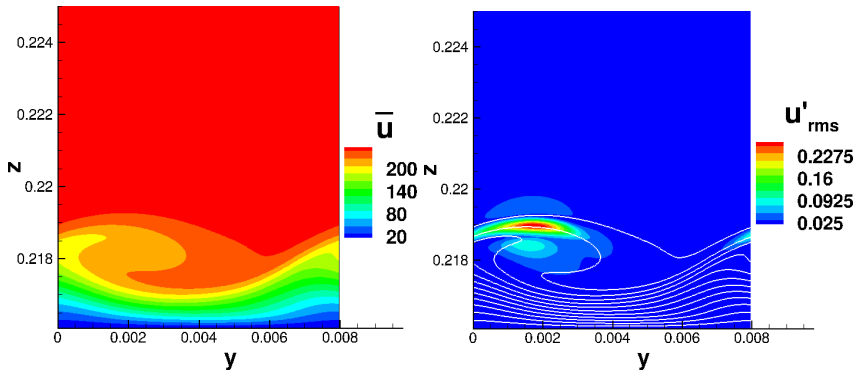

(a) (b)

FIGURE 2. (*a*) Mean and (*b*) time-RMS distributions of chordwise velocity (u_x) at the inlet of the DNS simulation. The white lines in the background of part (b) are the contours of mean chordwise velocity.

with the wall temperature prescribed to be equal to the laminar adiabatic temperature. Periodic boundary conditions are used in the spanwise direction.

The total number of grid points is 8461, 240, and 374 in the streamwise, spanwise, and wall-normal directions, respectively. The grid is clustered at streamwise locations within breakdown and turbulent regions. The computational grid resolution in the late-transitional and turbulent regions is comparable to, if not finer than, those reported in the literature in the context of previous simulations of turbulent wall-bounded flows using comparable numerical algorithms (Martín 2007). In the spanwise direction, the grid is uniformly distributed and the domain is limited to one single wavelength, λ_y, of the primary stationary crossflow vortex.

1.2. *Assessment of acoustic boundary conditions*

The boundary conditions of the DNS are specifically designed to inject instability waves (with the exact modal shape) at the inlet and minimize acoustic reflections at numerical boundaries. Both previous and current simulations show that strong acoustic disturbances (relative to the amplitude of the introduced secondary instability waves) with frequencies as low as 100 Hz (i.e., nearly 625 times lower than the secondary mode frequency of 62.5 kHz) are generated within the boundary layer near the transition zone (Figure 4).

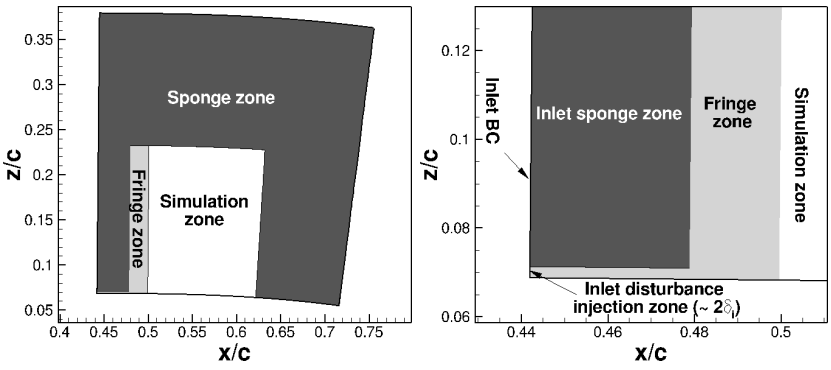

(a) (b)

FIGURE 3. Sketch of the simulation domain with boundary conditions that are designed specifically for injecting instability waves at the inlet and minimizing acoustic reflections at numerical boundaries. (a) Overall view; (b) zoomed-in view near the inlet.

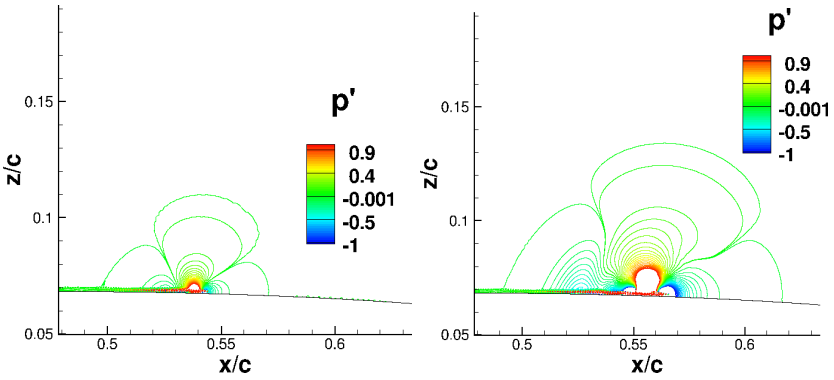

(a) (b)

FIGURE 4. Contours of pressure disturbances at two different time instances indicating the propagation of strong acoustic disturbances generated near the transition zone.

To assess the effectiveness of DNS boundary conditions in absorbing any generated acoustic waves, two-dimensional (2D) acoustic simulations are conducted using spatially compact and temporally harmonic forcing along with the same streamwise wall-normal boundary conditions and freestream conditions as the DNS case to be calculated. The following harmonic forcing function is introduced in the streamwise momentum equation

$$f(x,z,t) = \varepsilon(\rho_\infty U_\infty^2/\delta_i)\, g(x,z)\, cos(\omega t). \tag{1.1}$$

The nondimensional amplitude, ε, is adjusted so that the fluctuations generated are small enough to remain linear but also large enough to ensure a satisfactory signal-to-noise ratio in the computed solution; $g(x,z)$ specifies the location of the concentrated layer of sources, which was chosen to be a compact function of the form

$$g(x,z) = sin^2\left(\pi\,\frac{x-x_1}{x_2-x_1}\right) * sin^2\left(\pi\,\frac{z-z_1}{z_2-z_1}\right) \qquad x_1 \le x \le x_2, z_1 \le z \le z_2. \tag{1.2}$$

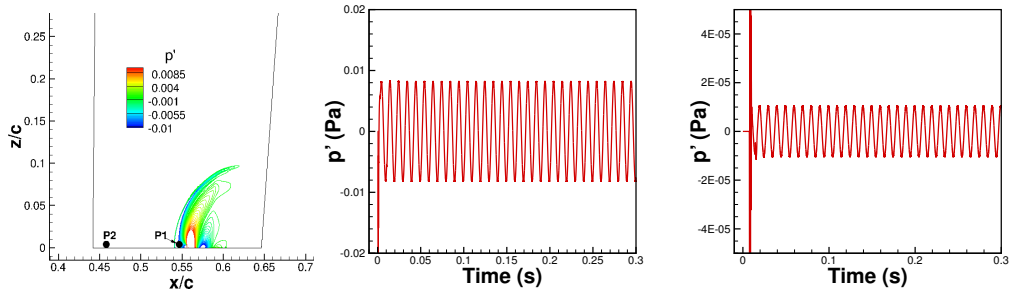

(a) (b) (c)

FIGURE 5. Two-dimensional acoustic simulation with harmonic forcing at 100 Hz for evaluating the efficacy of the sponge boundary condition. (a) Contours of instantaneous pressure disturbances indicating the forcing location and pattern; (b) typical probe signal close to the forcing location (indicated by P1 in (a)); (c) typical probe signal far upstream of the forcing location close to the vortex injection zone (indicated by P2 in (a)).

The 2D simulations use the DNS mesh within the $x-z$ plane with the boundary-layer region stripped off and with a straightened wall. The height of disturbance injection zone ($\approx 2\delta_i$) at the inlet is kept the same as the DNS domain to monitor the level of reflection due to the Dirichlet boundary condition applied in this small region. x_1, x_2, z_1 and z_2 are chosen such that the forcing is located within the region where transition occurs in the DNS domain.

Figure 5(a) shows the generation and propagation of acoustic disturbances due to forcing at 100 Hz, and Figure 5(b,c) shows typical probe signals near the forcing location and close to the inlet in the disturbance injection zone, respectively. The harmonic signals at large time indicate that numerical reflection at the boundary is minimal. Similar probe signals are observed for simulations with forcing at higher frequencies, indicating the robustness of the chosen boundary condition in minimizing numerical reflection of acoustic waves, at least for frequencies of 100 Hz and above.

Simulations were also conducted with a pulsed forcing to ensure that the signal returned to an undisturbed condition following the passage of the transient pulse emanating from the source region. No extraneous pulses indicating internal reflections were noted in the signal. The above findings from the acoustic computations are a strong indicator that the artificial boundary conditions used at inflow, free stream, and outflow are effectively serving their purpose.

2. Transition prediction in a swept-wing boundary layer

In this section, DNS results of laminar breakdown initiated by the secondary instability of stationary crossflow vortices are presented. We focus on comparing results between the DNS and the nonlinear PSE during both the linear and nonlinear phases of the secondary mode as well as on highlighting several important features of crossflow transition due to secondary instabilities.

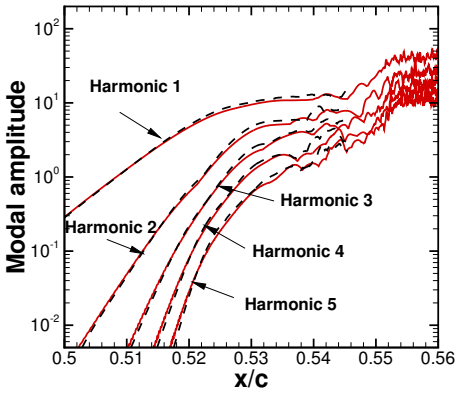

FIGURE 6. Chordwise development of secondary instability modes of the maximum chordwise velocity during the strongly nonlinear phase and laminar breakdown. The modal amplitude is measured in terms of the maximum of the root-mean-square streamwise velocity fluctuation over the local cross-section of the underlying crossflow vortex. The red curves correspond to DNS results and the black dash curves denote the nonlinear PSE computation.

2.1. *Comparison with PSE*

PSE computations for the developments of linear and nonlinear secondary instability modes are carried out solving the parabolized stability equations as implemented in the Langley Stability and Transition Analysis Codes (LASTRAC) (Chang 2004). In the current study, 16 harmonics of the fundamental frequency were included in the nonlinear PSE simulations of the secondary mode evolution and the spatial grid included 97 points over a single spanwise wavelength of the stationary mode and 281 points in the surface-normal direction.

Figure 6 shows the streamwise development of secondary instability modes of the maximum chordwise velocity during the strongly nonlinear phase and laminar breakdown, and Figure 7 shows the normalized time-RMS distributions of chordwise velocity at selected chordwise stations. Figures 6 and 7 show that the nonlinear PSE compares well with DNS in terms of modal amplitudes not only in the upstream region where the instability undergoes linear growth, but also during the strongly nonlinear phase where the evolution of modal amplitudes deviates from the linear growth and shows a quasi-saturated behavior. The flow structures tracked by PSE closely mimic those obtained by DNS up to the quasi-saturated regions ($x/c = 0.5452$).

Given that the quasi-saturation behavior of modal amplitude is followed by an abrupt increase in the modal amplitude that nearly coincides with the location of the abrupt rise in skin friction, the PSE is a valuable tool for predicting the location of transition onset.

2.2. *Laminar breakdown of stationary crossflow vortices*

Figure 8 displays the streamwise development of the skin friction coefficient averaged in time and spanwise coordinate. Due to the limited length of the computation thus far, the average in time is limited to 57 periods of the secondary wave. The skin friction

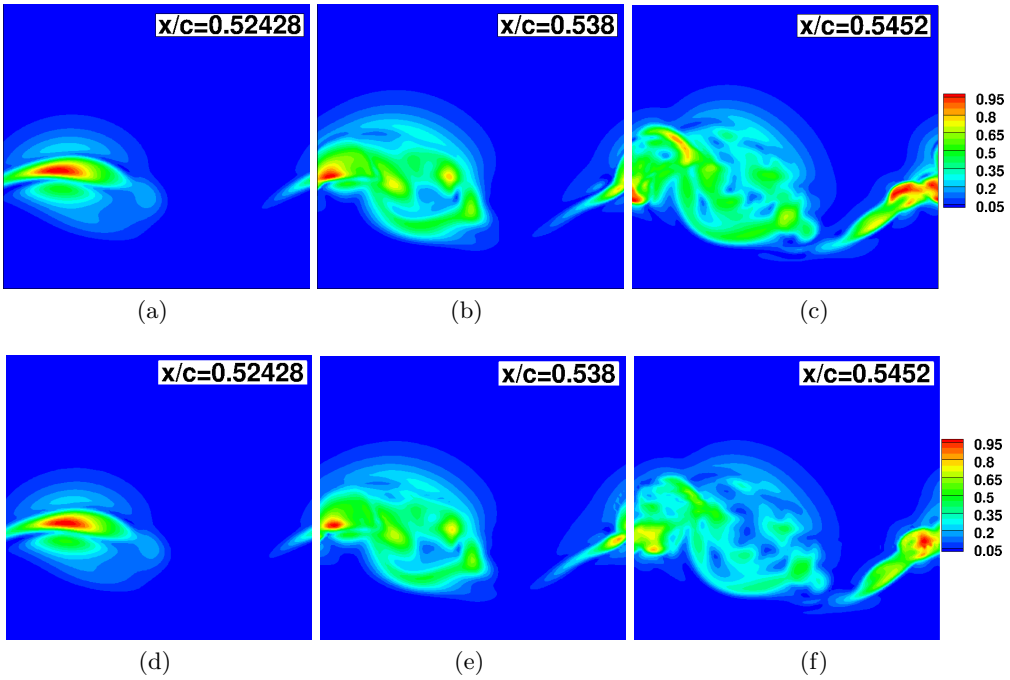

FIGURE 7. Time-RMS distributions of chordwise velocity at selected chordwise stations. The maximum RMS of chordwise velocity has been normalized to unity. (*a-c*) DNS results; (*d-f*) PSE results.

maintains a laminar level until $x/c \approx 0.554$, where it starts to rise rapidly, indicating the onset of transition. The abrupt rise in C_f in the current simulation appears consistent with the experimental observations at DLR for a transition triggered by a secondary high-frequency instability (Bippes 1999). The onset of transition approximately coincides with the peak location of the modal amplitude of the secondary instability mode shown in Figure 6. At a location slightly downstream of the onset ($x/c \approx 0.56$), the skin-friction reaches a maximum value that is close to ten times that of the laminar level. Downstream of the location of maximum skin friction, the skin-friction curve follows the prediction based on van Driest (1956) for a 2D turbulent boundary layer. At $x/c \approx 0.62$, the mean chordwise velocity profile relaxes to a fully turbulent profile that shows a (narrow) logarithmic region and, furthermore, conforms well with the incompressible law-of-the-wall profile following the van Driest transformation (Figure 9).

To show the spanwise distribution of the transition front, contours of time-averaged wall shear distribution are plotted in Figure 10. The mean wall-shear contours clearly display a noticeable nonuniformity in the spanwise direction. Spanwise periodic extension of the computed transition front shows a sawtooth pattern similar to that noted during surface flow visualization of swept-wing boundary layers when the transition process is dominated by stationary crossflow instability (as opposed to traveling modes, which lead to smoother spanwise variations in the transition front) (Reibert 1996). The half-angle of the turbulent wedge is approximately 7° to 8°, which is nearly the same as that observed by Choudhari *et al.* (2013) in the case of swept-wing transition due to a Z-mode of

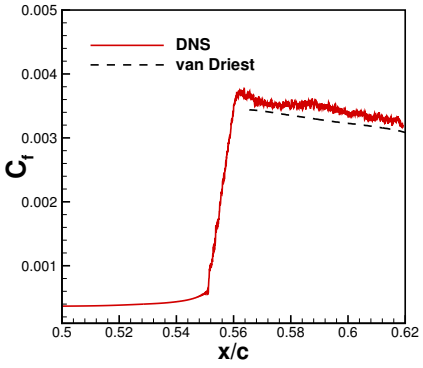

FIGURE 8. Evolution of skin friction coefficient averaged in time and span along the chordwise direction.

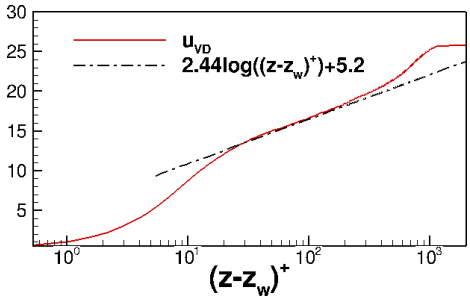

FIGURE 9. Van-Driest transformed chordwise velocity, $\overline{u}_{VD}$, at $x/c \approx 0.62$, with $\overline{u}_{VD} \equiv (1/u_\tau)\int_0^{u_x}(\overline{T}_w/\overline{T})^{1/2}du_x$.

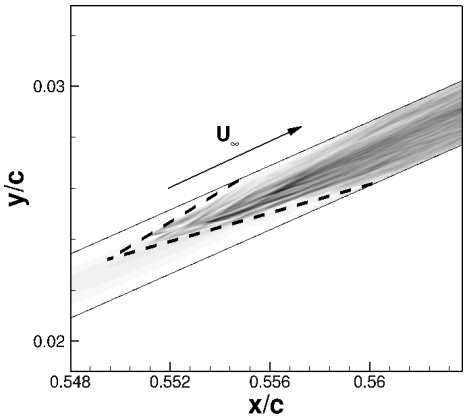

FIGURE 10. Contours of time-averaged wall shear from the DNS, viewed in the x-y plane, with black color indicating high shear and white color indicating low shear. Black dash lines indicate the saw tooth curve marking the onset of increased skin friction.

secondary instability and also close to the measured range of angles for the spreading of a turbulent disturbance (Fischer 1972) and the computed spreading angle for a turbulent spot (Strand & Goldstein 2011).

3. Summary

Direct numerical simulation of transition due to secondary instability of stationary crossflow vortices in a swept-wing boundary layer has been performed for a realistic airfoil configuration that is relevant to subsonic transports with an extended region of natural laminar flow. An inlet boundary condition is carefully designed to allow for accurate injection of instability wave modes and minimization of acoustic reflections at numerical boundaries.

Both linear and nonlinear growth of the secondary instability is observed prior to the

laminar breakdown process in the DNS. Nonlinear PSE compares well with the DNS in terms of modal amplitudes and modal shape during the strongly nonlinear phase of the secondary instability mode. During the transition process, the skin friction coefficient rises rather rapidly across just a few wavelengths of the secondary instability mode. The wall shear distribution shows a sawtooth pattern that is analogous to the previously documented surface flow visualizations of transition due to stationary crossflow instability. Fully turbulent features are observed in the downstream region of the flow.

Acknowledgments

The authors wish to thank Prof. Sanjiva Lele and the Center for Turbulence Research at Stanford University for their hospitality and technical support. The authors would also like to thank Prof. Pino Martín of the University of Maryland for providing the original code which has been modified for the current study. The simulations have been conducted using the Pleiades supercomputer of the NASA Advanced Supercomputing (NAS) Division and the Stampede supercomputer of the Extreme Science and Engineering Discovery Environment (XSEDE), which is supported by National Science Foundation grant number OCI-1053575.

REFERENCES

Belisle, M. J., Neale, T. P., Reed, H. L. & Saric, W. S. 2010 Design of a swept-wing laminar flow control flight experiment for transonic aircraft. *AIAA Paper 2010-4381*.

Bippes, H. 1999 Basic experiments on transition in three-dimensional boundary layers dominated by crossflow instability. *Prog. Aero. Sci.* **35** (4), 363–412.

Bodony, D. J. 2006 Analysis of sponge zones for computational fluid mechanics. *J. Comput. Phys.* **212** (2), 681–702.

Breuer, M. 2007 *Large-Eddy Simulation for Acoustics*. Cambridge University Press.

Chang, C. L. 2004 *Langley Stability and Transition Analysis Code (LASTRAC) Version 1.2 User Manual*. NASA/TM-2004-213233.

Choudhari, M. M., Chang, C. L., Streett, C. L. & Balakumar, P. 2003 Integrated transition prediction: A case study in supersonic laminar flow control. *AIAA Paper 2003-0973*.

Choudhari, M. M., Li, F., Duan, L., Chang, C.-L., Carpenter, M. H., Streett, C. L. & Malik, M. R. 2013 Towards bridging the gaps in holistic transition prediction via numerical simulations. *AIAA Paper 2013-2718*.

van Driest, E. R. 1956 Problem of aerodynamic heating. *Aero. Eng. Rev.* **15**, 26–41.

Duan, L., Choudhari, M. M. & Li, F. 2013 Direct numerical simulation of transition in a swept-wing boundary layer. *AIAA Paper 2013-2617*.

Fischer, M. C. 1972 Spreading of a turbulent disturbance. *AIAA J.* **10** (7), 957–959.

Jiang, L., Choudhari, M. M., Chang, C. L. & Liu, C. 2006 Direct numerical simulations of transition in a supersonic boundary layer. *AIAA Paper 2006-3224*.

Li, F., Choudhari, M. M., Carpenter, M. H., Malik, M. R., Chang, C. L. & Streett, C. L. 2010 Roughness based crossflow transition control for a swept airfoil design relevant to subsonic transports. *AIAA Paper 2010-4380*.

Li, F., Choudhari, M. M., Chang, C. L., Streett, C. L. & Carpenter, M. H.

2011 Direct numerical simulations of transition in a supersonic boundary layer. *AIAA J.* **49**, 520–529.

Malik, M. R., Li, F., Choudhari, M. M. & Chang, C. L. 1999 Secondary instability of crossflow vortices and swept-wing boundary-layer transition. *J. Fluid Mech.* **399**, 85–115.

Martín, M. 2007 DNS of hypersonic turbulent boundary layers. Part I: Initialization and comparison with experiments. *J. Fluid Mech.* **570**, 347–364.

Mayer, C. S. J., Terzi, D. V. & Fasel, H. F. 2011 Direct numerical simulation of complete transition to turbulence via oblique breakdown at Mach 3. *J. Fluid Mech.* **674**, 5–42.

Moin, P. & Kim, J. 1982 Numerical investigation of turbulent channel flow. *J. Fluid Mech.* **118**, 341–377.

Nagarajan, S., Lele, S. K. & Ferziger, J. H. 2007 Leading edge effects in bypass transition. *J. Fluid Mech.* **572**, 471–504.

Ovchinnikov, V., Choudhari, M. M. & Piomelli, U. 2008 Numerical simulations of boundary layer bypass transition due to high-amplitude free-stream turbulence. *J. Fluid Mech.* **613**, 135–169.

Reibert, M. S. 1996 *Nonlinear stability, saturation, and transition in crossflow-dominated boundary layers.* PhD thesis, Arizona State University.

Rist, U. & Fasel, H. 1995 Direct numerical simulation of controlled transition in a flat plate boundary layer. *J. Fluid Mech.* **298**, 211–248.

Sayadi, T., Hamman, C. W. & Moin, P. 2013 Direct numerical simulation of complete h-type and k-type transitions with implications for the dynamics of turbulent boundary layers. *J. Fluid Mech.* **724**, 480–509.

Spalart, P. R. 1988 Direct simulation of a turbulent boundary layer up to $Re_\theta = 1410$. *J. Fluid Mech.* **187**, 61–98.

Strand, J. S. & Goldstein, D. 2011 Direct numerical simulations of riblets to constrain the growth of turbulent spots. *J. Fluid Mech.* **688**, 267–292.

Washburn, A. 2011 Drag reduction status and plans laminar flow and AFC. *AIAA Aero Sciences Meeting, Orlando, FL.*

Wu, X. & Moin, P. 2009 Direct numerical simulation of turbulence in a nominally zero-pressure-gradient flat-plate boundary layer. *J. Fluid Mech.* **630**, 5–41.